Journal of ELECTRONIC MATERIALS
DOI: 10.1007/s11664-013-2471-9

Thermoelectric Generators for Automotive Waste Heat Recovery Systems Part I: Numerical Modeling and Baseline Model Analysis

SUMEET KUMAR,[1,3] STEPHEN D. HEISTER,[1] XIANFAN XU,[1] JAMES R. SALVADOR,[2] and GREGORY P. MEISNER[2]

1.—School of Mechanical Engineering, Purdue University, West Lafayette, IN, USA. 2.—General Motors Global R&D, Warren, MI, USA. 3.—e-mail: kumar94@purdue.edu

A numerical model has been developed to simulate coupled thermal and electrical energy transfer processes in a thermoelectric generator (TEG) designed for automotive waste heat recovery systems. This model is capable of computing the overall heat transferred, the electrical power output, and the associated pressure drop for given inlet conditions of the exhaust gas and the available TEG volume. Multiple-filled skutterudites and conventional bismuth telluride are considered for thermoelectric modules (TEMs) for conversion of waste heat from exhaust into usable electrical power. Heat transfer between the hot exhaust gas and the hot side of the TEMs is enhanced with the use of a plate-fin heat exchanger integrated within the TEG and using liquid coolant on the cold side. The TEG is discretized along the exhaust flow direction using a finite-volume method. Each control volume is modeled as a thermal resistance network which consists of integrated submodels including a heat exchanger and a thermoelectric device. The pressure drop along the TEG is calculated using standard pressure loss correlations and viscous drag models. The model is validated to preserve global energy balances and is applied to analyze a prototype TEG with data provided by General Motors. Detailed results are provided for local and global heat transfer and electric power generation. In the companion paper, the model is then applied to consider various TEG topologies using skutterudite and bismuth telluride TEMs.

Key words: Thermoelectric generators, waste heat recovery, automotive exhaust, skutterudites

INTRODUCTION

Substantial thermal energy is available from the exhaust gas in modern automotive engines. Two-thirds of the energy from combustion in a vehicle is lost as waste heat, of which 40% is in the form of hot exhaust gas.[1,2] Use of TEGs has the potential to recover some of this waste energy in the exhaust stream, potentially improving fuel economy (FE) by as much as 5%. A comprehensive theoretical study concluded that a TEG powered by exhaust heat could meet the electrical requirements of a medium-sized vehicle.[1]

Over the last several decades, alloy-based thermoelectric (TE) materials including Bi_2Te_3—Sb_2Te_3 and Si-Ge systems have been extensively studied for use in their different temperature ranges.[3–5] As the temperatures of automobile exhaust gases are typically in the range of 400°C to 800°C, high-temperature TE devices are required for at least a part of the flow path. Established TE semiconductors exhibit poor figures of merit when operating temperatures exceed 500°C.[4,5] Crane et al.[6] have implemented

(Received September 10, 2012; accepted January 4, 2013)

Published online: 20 February 2013

two-stage segmented TE elements based on half-Heusler alloy (Zr, Hf) near the hot gas inlet and Bi_2Te_3 elements near the exit of a TEG prototype designed for a 3-L BMW inline six-cylinder engine. Meisner et al.[7] have employed high-temperature skutterudites for a prototype designed for General Motors Suburban. While TEMs based on $FeSi_2$[8] and Pb-Te[9] have been used for prototypical exhaust generators, recent research has explored new and more efficient options including nanoscale materials[3] employing superlattice structures,[3] nanowires,[10,11] quantum dots,[3] and nanostructured-bulk alloys.[3] Increased thermoelectric efficiency has been realized by taking advantage of electronic band structure engineering[3,11] and phonon engineering.[3,10] Multiple-filled skutterudites[12,13] have promised higher ZT (>1) values in the temperature range of 300°C to 600°C and exhibit superior mechanical strength, and are therefore of primary interest in the present study.

TEGs have historically been employed in specialized military and space applications.[14] Thermoelectric converters have been used to power deep-space probes since the 1950s due to the ease of scalability and the overall simplicity as compared with alternative approaches.[15] However, recent improvements in energy conversion efficiencies[3,12,13,16] of TE materials, combined with increased interest in energy efficiency and fuel economy, have led to an unprecedented increase in research into their potential deployment in environments where thermal energy is virtually free such as solar radiation,[17,18] automobile exhaust,[19–21] and gas turbine and diesel cycle cogeneration systems.[22] Researchers in Japan[23] have been working on oxide TEGs as a topping cycle to remove some of the heat from the steam in incinerators to curtail use of expensive turbines. While current projected TEG efficiencies are low (typically less than 5%), the fact that the energy available is essentially free and that the units are mechanically simple has fostered renewed interest. Morelli[24] assessed critical issues to be considered for an exhaust gas generator design such as location, heat transfer from exhaust gas, generator mass, thermoelectric material stability, and overall environmental friendliness. This work showed that the internal finning and diffuser arrangement in the TEG system are important design considerations for minimizing the temperature difference between the hot gas and the hot side of the thermoelectric elements.

The first TEG prototypes were constructed in the late 1960s using Pb-Te- and Ge-Bi-Te-based alloys.[25,26] In the second half of the last century, prototypes were developed by Porsche,[8] Hi-Z,[27,28] Nissan Motors,[29] and Clarkson University in collaboration with General Motors.[30,31] All of these TEGs used exhaust gases and engine coolant as the heat source and sink, respectively. Karri et al.[32] highlighted the use of a thermoelectric generator placed in the exhaust stream of a sports utility vehicle (SUV) and a stationary, compressed natural gas (CNG)-fueled engine generator set. Researchers at BMW obtained 200 W of electrical power from a TEG comprising 24 Bi_2Te_3 modules in a 3-L-engine BMW 535i vehicle driven at 130 km/h.[33,34] The benchtest of BSST's cylindrical TEG, designed for the Ford Lincoln MKT and the BMW ×6, reported electrical power generation exceeding 700 W.[35] General Motors noted that achieving 350 W and 600 W is possible in a Chevrolet Suburban under city and highway driving conditions, respectively, with an average of 15 kW of heat energy available over the drive cycle.[36] Meisner outlined the progress by General Motors in the development of various phases of TEG prototypes using Bi-Te and skutterudite modules in the Chevrolet Suburban vehicle.[7,37] Numerical models[38–40] have been developed to assess TEG performance at various engine operating conditions using plate-fin heat exchangers and commercial Bi_2Te_3-based modules. Crane et al.[41] have developed steady-state and transient models of high-power-density TEGs. Hsiao et al.[42] built a one-dimensional thermal resistance model for a TEG and found that performance on the exhaust pipe is better than on the radiator.

A diesel engine TEG application modeled by Espinosa et al.[20] employed Mg_2Si/Zn_4Sb_3 for high temperatures followed by Bi_2Te_3 for low temperatures. Matsubara[20,43] demonstrated a highly efficient thermoelectric stack composed of segmented legs using highly doped $CoSb_3$ and filled skutterudite RM_4Sb_{12} (R = Ce, Yb; M = Co, Fe, Ni, Pt, Pd) and HZ-14 (based on Bi_2Te_3 from HI-Z Technology, Inc.) TEMs and achieved a 5% to 10% efficiency depending on engine operating conditions. The operating temperature was in the range of 350°C to 750°C, and it was demonstrated that ZT = 1.5 to 2.0 will be needed to attain a goal of 10% overall efficiency.

A number of models[44–50] have been applied for TEG analysis, with varying levels of sophistication. The modeling challenges include the consideration of heat flow through heat exchangers and into/through TEMs while taking into account the temperature dependence of the TEM performance. Thermal resistances across the various material interfaces,[44,45] electrical load impedance balancing, and axial gradients in temperature due to heat extraction are all important considerations. Large changes in bulk gas temperature in the axial direction are a challenge for maintaining the TE material performance over a wide range of operating conditions. As the engine performance is tightly coupled to the overall pressure ratio, heat exchanger finning arrangements must not create an undue pressure drop in the TEG, or performance gains from electrical power will be offset by corresponding losses in the basic Otto cycle. In many automotive applications, the Reynolds numbers within the flow path place the flow in a transition region between laminar and turbulent behavior, thereby complicating flow analysis. Finally, cost is a

major driver for the automotive industry; a target incremental cost less than US $1000/unit will likely be required for commercial application of the technology. However, the additional gain in fuel economy by 5% may offset these high equipment costs.

The primary objective of the present study is to develop a comprehensive tool for investigating TEG performance over a wide range of design and operating conditions. The model must provide a simultaneous solution of coupled thermal–electrical energy fluxes for accurate prediction of electrical power generation, temperature profiles, and thermal energy fluxes. The following section provides a description of model elements and validation of the local and global energy balances. The tool is then applied to the General Motors prototype as a baseline model to understand the dependence of output parameters on various system elements.

MODEL DESCRIPTION

The rectangular configuration of a TEG is presented in Fig. 1. TEMs are mounted on the top and the bottom surface and arranged uniformly over the available surface (80% of total surface area) as shown. The remaining 20% area and the lateral walls are thermally insulated to minimize heat leakage. A plate-fin heat exchanger with fins running along the TEG length is shown in Fig. 2. The cold-side temperature of the modules is maintained by the engine coolant system. The entry and exit ports of the box are connected to the exhaust pipe of the automobile.

TEG Modeling

Steady-state analysis of hot exhaust gas flow along the TEG length was performed for the current study. The variation in fluid properties and thermoelectric properties with temperature is considered along the flow direction. Since the TEG is symmetric with respect to its height, only half of the domain is simulated. The TEG domain is discretized into small control volumes (CVs) along the length as shown in Fig. 2. The gas temperature is assumed to be uniform inside a CV. The available hot-side surface area is designated as 80% of the base area A_{Base} in a CV, and is assumed to be covered by a uniform distribution of TEMs represented as A_{module}. The leg dimensions and number density of TE couples (n- and p-legs) may vary with the TE materials, temperature ranges of operation, and cost.

$$\eta_{\text{CV,TEC}} = \text{NumberDensity} * A_{\text{Module}}. \tag{1}$$

Here, the number density of TE couples (n- and p-legs) is known a priori for TEMs as provided by General Motors (Table I), and hence the approximate number of TE n–p legs can be computed for each CV area as $\eta_{\text{CV,TEC}}$. The remaining 20% of A_{Base} is considered to be covered by thermal insulation, represented as A_{Ins}

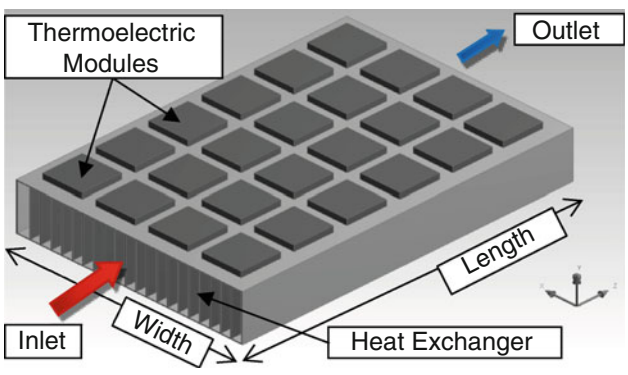

Fig. 1. Schematic of a rectangular TEG model.

Thermal Resistance Network

The smallest possible configuration of a TEG can be assumed as a system composed of a TE couple (one n- and one p-leg), the plate-fin heat exchanger at the hot-side junction, and the engine coolant system mounted near the cold junction as shown in Fig. 3. A CV can be modeled as a parallel combination of numerous such small systems calculated by Eq. (1). An equivalent thermal resistance network for a CV is represented in Fig. 4.

The hot-side heat exchanger assembly can be modeled as an effective thermal resistance given by Eq. (2). Fin resistance modeling details for a plate-fin heat exchanger assembly can be found in the work by Incropera.[51] Here, η_0 is the overall fin effectiveness and A_t is the total area of the heat exchanger, i.e., the fin surface area and the unfinned base area in a CV. $\overline{h}_g$ is the average heat transfer coefficient based on the fin channel Reynolds number. The thermal resistances for the top surface of the device, ceramic slab, thermal grease, and thermal insulation can be given by Eqs. (3–6).

$$R_{\text{fin,eq}} = 1/\left(\eta_0 \overline{h}_g A_t\right), \tag{2}$$

$$R_{\text{TEG,base}} = t_{\text{base}}/(k_{\text{base}} A_{\text{base}}), \tag{3}$$

$$R_{\text{ceramic}} = t_{\text{ceramic}}/(k_{\text{ceramic}} A_{\text{Module}}), \tag{4}$$

$$R_{\text{grease}} = t_{\text{grease}}/\left(k_{\text{grease}} A_{\text{Module}}\right), \tag{5}$$

$$R_{\text{Ins}} = t_{\text{Ins}}/(k_{\text{Ins}} A_{\text{Ins}}). \tag{6}$$

Radiative heat transfer is considered for hot exposed surfaces, i.e., insulated top surface and the part of the TEM's hot surface not covered by the TE legs. The expressions for the radiative heat transfer coefficient h_{rad} and the radiation resistances for these surfaces are given by Eqs. (7–10). Here, A_{TEC} and A_{Ins} are the areas of a TE couple and thermally

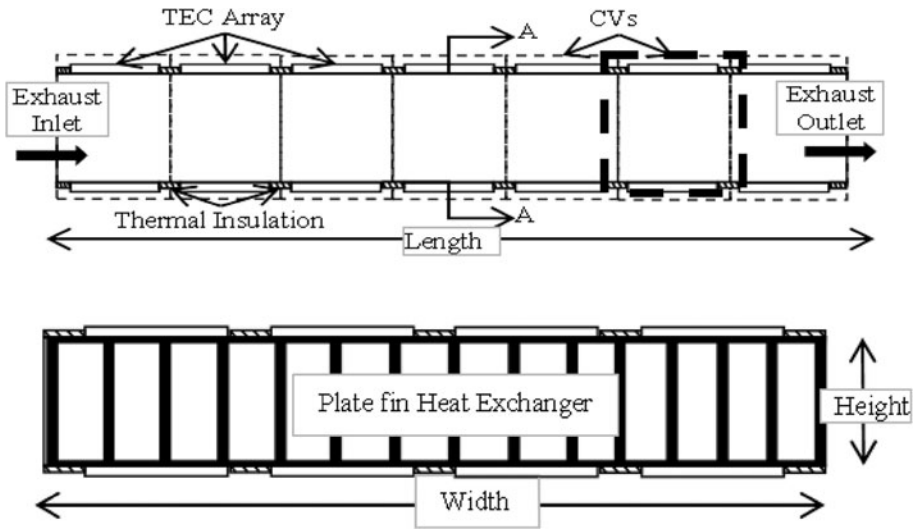

Fig. 2. Side view (top) with representation of a control volume (CV) in the dashed box and front view (bottom) showing the integrated plate-fin heat exchanger.

Table I. User inputs and baseline configuration

Parameter	Value	Unit
Geometry		
Thermoelectric generator volume	0.003592	m^3
Exhaust inlet and outlet pipe diameter	0.0635	m
Dimensions for rectangular topology (length, height, width)	(0.413, 0.038, 0.224)	(m, m, m)
Fins (copper) (thickness, spacing)	(0.0033, 0.00635)	(m, m)
Thermoelectric module		
Skutterudite-based module (cross-section, height)	(0.0508 × 0.0508, 0.007)	(m^2, m)
TEC (N_{TEC}, cross-section, height)	(32, 0.004 × 0.004, 0.004)	(–, m^2, m)
ε_{Module} (ceramic)	0.55	–
Thermoelectric material	$Ba_{0.08}La_{0.05}Yb_{0.04}Co_4Sb_{12}$ (n)[12]	–
	$DD_{0.76}Fe_{3.4}Ni_{0.6}Sb_{12}$ (p)[13]	–
Fluid		
Air properties	Ideal gas formulation (EES)	–
Materials		
Thermal grease (Grafoil laminate) thickness	0.001	m
Thermal conductivity	5	W m^{-1} K^{-1}
Thermal insulation (Min-K) thickness	0.002	m
Thermal conductivity	0.0334	W m^{-1} K^{-1}
ε_{Ins}	0.75	–
TEG model base (copper) thickness	0.008	m
Thermal conductivity	401	W m^{-1} K^{-1}

insulated surface in a control volume, respectively. σ is the Stefan–Boltzmann constant, and ε is the emissivity of the radiating surfaces of the respective materials.

$$R_{rad,Ins} = 1/\left(h_{rad,Ins}A_{Ins}\right), \quad (7)$$

$$R_{rad,TEM} = 1/\left[h_{rad,TEM}\left(A_{Module} - \eta_{CV,TEC}A_{TEC}\right)\right], \quad (8)$$

$$h_{rad,TEM} = \varepsilon_{TEM}\sigma\left(T_5^3 + T_5^2T_8 + T_5T_8^2 + T_8^3\right), \quad (9)$$

$$h_{rad,Ins} = \varepsilon_{Ins}\sigma\left(T_3^3 + T_3^2T_8 + T_3T_8^2 + T_8^3\right). \quad (10)$$

The thermoelectric properties of n- and p-legs are functions of temperature. The properties are averaged over the junction temperatures. The Seebeck coefficient (α), thermal conductance (K), and internal electrical conductance (r_{el}) can be computed for a TE couple as given by Eq. (11–13). L denotes the length of a thermoelectric leg (n or p), and A denotes the cross-sectional area. Subscripts "n" and "p" denote the corresponding n or p thermoelectric materials. λ and ρ are thermal conductivity and electrical resistivity, respectively.

$$\alpha_{TEC} = \alpha_p - \alpha_n, \quad (11)$$

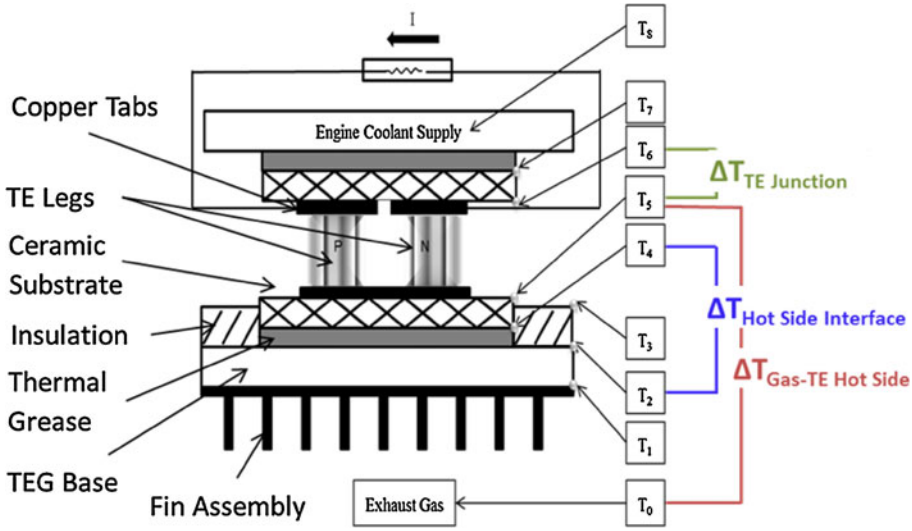

Fig. 3. Representation of a TE couple (one *n*- and one *p*-leg) with fins at the hot side and coolant at the cold side. The TE couple is connected to an external electrical load for electrical power generation.

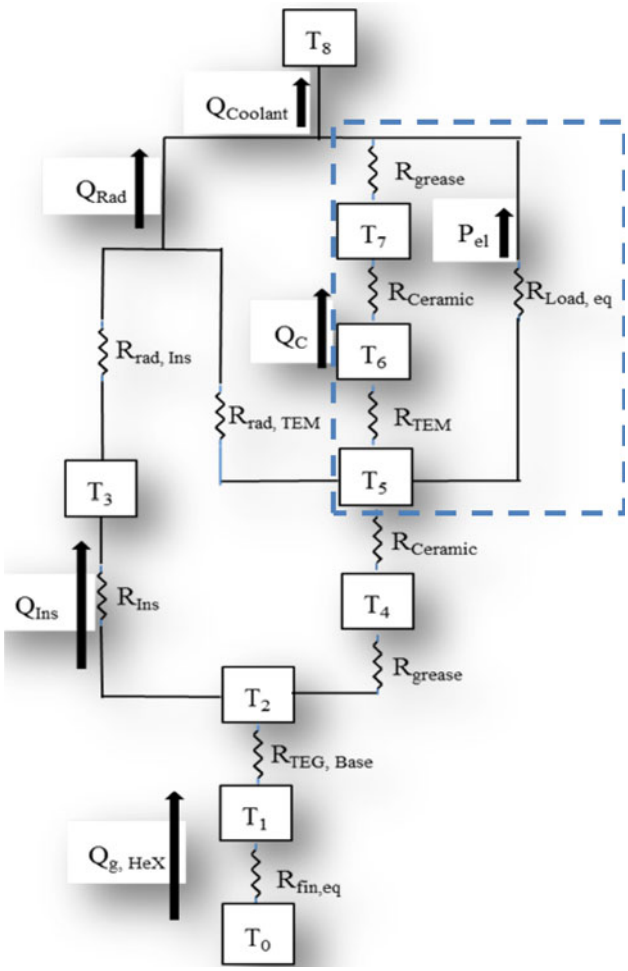

Fig. 4. Equivalent thermal resistance network for a CV. The dashed box encloses the thermoelectric components. The block arrows signify thermal and electrical energy flows through the circuit.

$$K_{\mathrm{TEC}} = \frac{\lambda_p A_p}{L_p} + \frac{\lambda_n A_n}{L_n}, \tag{12}$$

$$\mathrm{r}_{\mathrm{el,TEC}} = \frac{L_p \rho_p}{A_p} + \frac{L_n \rho_n}{A_n}, \tag{13}$$

$$ZT_{\mathrm{TEC}} = \frac{\langle \alpha_p - \alpha_n \rangle^2 T}{\left[\langle \rho_p \lambda_p \rangle^{1/2} + \langle \rho_n \lambda_n \rangle^{1/2}\right]^2}. \tag{14}$$

Similarly, the figure of merit ZT for a TE couple can be computed as shown in Eq. (14).[10] Equivalent thermal resistances for thermoelectric components can be defined by manipulation of equations. Across the thermoelectric couple junction, the open-circuit voltage is defined as

$$V_{\mathrm{oc}} = \alpha_{\mathrm{TEC}}(T_5 - T_6). \tag{15}$$

Here, T_5 and T_6 are junction temperatures. The electrical current I through the thermoelectric couple, connected to an external electrical load resistance ($r_{\mathrm{el,L}}$), can be specified as

$$I = \frac{V_{\mathrm{oc}}}{\left(r_{\mathrm{el,L}} + r_{\mathrm{el,TEC}}\right)}. \tag{16}$$

Hence, the heat transfer from the hot side and cold side of the thermoelectric couple junction system[10] are given as

$$Q_{\mathrm{H}} = \alpha_{\mathrm{TEC}} T_5 I - \frac{1}{2} I^2 r_{\mathrm{el,TEC}} + K_{\mathrm{TEC}}(T_5 - T_6), \tag{17}$$

$$Q_C = \alpha_{TEC} T_6 I + \frac{1}{2} I^2 r_{el,TEC} + K_{TEC}(T_5 - T_6). \quad (18)$$

After combining Eqs. (15) and (16) and taking the difference of Eqs. (17) and (18), the electrical power output across the external electrical load resistance is given by Eq. (19). Here, a TE couple is assumed to be connected to an external electrical load having the same magnitude as the internal electrical resistance, i.e., $r_{el,L} = r_{el,TEC}$.

$$P_{el,TEC} = Q_H - Q_C = I^2 r_{el,L}. \quad (19)$$

Hence, the thermal resistances are modeled to complete the network branches along path 5 to 8 shown in Fig. 4. Since, the thermal energy transfer through these thermoelectric couples is in a parallel fashion, their contribution in a control volume can be summed up in an equivalent module resistance given as

$$R_{TEM} = \frac{(T_5 - T_6)}{\eta_{CV,TEC}(Q_H - P_{el,TEC})}, \quad (20)$$

whereas the equivalent thermal load resistance for branch 5–8 can be written as

$$R_{Load,eq} = \frac{(T_5 - T_8)}{\eta_{CV,TEC} P_{el,TEC}}. \quad (21)$$

Similarly, the thermal resistances in branches 0–2 and 2–8 (thermal insulation and TEM) in Fig. 4 can be added up together for a thermal circuit as

$$R_{02} = R_{fin,eq} + R_{TEG,Base}, \quad (22)$$

$$R_{28,Ins} = R_{Ins} + R_{rad,Ins}, \quad (23)$$

$$R_{28,TEM} = R_{grease} + R_{ceramic} + \left(\begin{array}{l} R_{rad,TEM}^{-1} + \\ (R_{TEM} + R_{ceramic} + R_{grease})^{-1} \\ + R_{Load,eq}^{-1} \end{array} \right)^{-1}. \quad (24)$$

Using the resistances in the top and bottom branches, an explicit expression for T_2 in terms of T_0 and T_8 can be derived as

$$T_2 = \frac{T_0 R_{02}^{-1} + T_8 \left(R_{28,Ins}^{-1} + R_{28,TEM}^{-1} \right)}{R_{02}^{-1} + \left(R_{28,Ins}^{-1} + R_{28,TEM}^{-1} \right)}. \quad (25)$$

For the current topology with symmetry, the gas bulk temperature at the end of each ith CV boundary can be computed from the CV energy balance as shown in Eq. (26). $Q_{g,HeX}$ is the heat energy transferred by the heat exchanger to the thermoelectric materials and the insulation. C_p is the specific heat capacity of gas, and $\dot{m}$ is the exhaust gas flow rate.

$$T_{g,i+1} = T_{g,i} - Q_{g,HeX} / \left((\dot{m}/2) C_p \right). \quad (26)$$

Pressure Drop Calculations

The fluid flow across the thermoelectric generator induces pressure drops throughout the TEG. The change in cross-section at the entry port, i.e., the exhaust inlet pipe to the TEG, and exit port lead to pressure drops or gains depending on the area ratios at these transitions. The pressure drop is calculated using Borda–Carnot correlations as shown in Eqs. (27) and (28).[52] Due to the turbulent flow pipe regime for mass flow rate of 20 g/s to 100 g/s (Re = 12,000 to 60,000), the flow transition between the exhaust pipe and TEG cross-section can be approximated as sudden expansion or contraction. The expressions for the pressure change across sudden expansion (Exp) and contraction (Con) from the area of section 1 to 2 are given by Eq. (27–29).

$$\Delta P_{Exp} = -d_{air} \frac{A_1}{A_2} \left(1 - \frac{A_1}{A_2} \right) v_1^2, \quad (27)$$

$$\Delta P_{Con} = \frac{1}{2} d_{air} \left(\frac{1}{\mu} - 1 \right)^2 \left(\frac{A_1}{A_2} \right)^2 v_1^2, \quad (28)$$

$$\mu = 0.63 + 0.37 \left(\frac{A_2}{A_1} \right)^3. \quad (29)$$

Here, v and d are the fin channel velocity and mass density of gas, respectively. The viscous drag effect on the fin surfaces adds to the pressure drop along the length of the TEG. The pressure drop across the heat exchanger assembly given in Eq. (30) is calculated by summing the pressure drops across each of the CVs. Using the friction factor f based on the Reynolds number inferred from the fluid flow regime, the hydraulic diameter of a fin channel for a given aspect ratio,[51] Δx_{CV} (the CV thickness), and v_{ch} (the fin channel gas velocity), the pressure drop per CV can be computed.

$$\Delta P_{HeX} = \sum_{CV} f \Delta x_{CV} d_{air} \frac{v_{ch}^2}{2}. \quad (30)$$

SOLUTION METHOD

Since the nonlinear thermal resistances depend on the thermoelectric material properties and its terminal temperatures, the temperatures in the thermal circuit must be solved in an iterative

manner. The thermoelectric properties and thermal resistances are updated at each iteration step until the temperatures do not change beyond a tolerance value (10^{-6}). The solution consists of an inner and an outer iteration loop, such that the outer iteration loop runs until the gas bulk temperature converges for each control volume. The inner loops run until the temperature and resistance values converge within a control volume based on the mean bulk gas temperature supplied by the outer iteration loop.

GM Baseline Model

The inputs chosen for the baseline analysis were taken from a General Motors (GM) prototype designed for a Chevrolet Suburban.[7,37] The property data for insulation, thermal grease, etc. were provided by GM (thermal insulation was Min-K sheets, thermal grease was Omega's high-temperature thermal paste). The geometrical specifications of the prototype and skutterudites modules from Marlow Industries were used for modeling the TEMs (Table I). For the Chevrolet Suburban exhaust, mass flow rates were found to vary from 20 g/s to 100 g/s with temperatures ranging from 400°C to 700°C when subjected to road loads comparable to those found in the typical federal test procedure. The average inlet conditions were $\dot{m}$ = 35 g/s and T_{in} = 550°C for the driving cycle.

Model Verification

The numerical code was verified for grid independence and global energy balance. The baseline configuration was run for the average inlet conditions of $\dot{m}$ = 35 g/s and T = 550°C for code verification. Electrical power was plotted for various grid sizes (N_x) ranging from as coarse as 2 to as fine as 128 elements along the flow direction, as shown in Fig. 5. A reasonable grid size of 100 gave a relative error of 10^{-5} as computed by Eq. (31). The subscript "$i-1$" stands for the coarser grid and "i" for the finer grid size.

$$Err_{\text{rel},i} = \frac{P_{\text{el},i-1} - P_{\text{el},i}}{P_{\text{el},i}} \times 100\%. \tag{31}$$

The code was also verified to ensure basic energy conservation principles by performing energy balance calculations on the baseline configuration. The enthalpy influx rate $\dot{H}_{\text{in}}$ was calculated by multiplying the air enthalpy at the inlet temperature of 550°C by the flow rate of 35 g/s. Similarly, the enthalpy outflow $\dot{H}_{\text{out}}$ was calculated at the exit temperatures. The enthalpy change $\Delta\dot{H} = \dot{H}_{\text{in}} - \dot{H}_{\text{out}}$ is the energy rate transferred by the gas to the generator. $\dot{Q}_{\text{coolant}}$ is the rate at which energy is rejected due to conduction from the cold side and radiative effects. $\dot{Q}_{\text{trf}}$ is the sum of the generated electrical power $\dot{P}_{\text{el}}$ and the heat rejection rate $\dot{Q}_{\text{coolant}}$. The energy imbalance was computed as the absolute error from the difference of $\dot{Q}_{\text{trf}}$ and $\Delta\dot{H}$. The relative error (%) for all the models analyzed was less than 0.052% for 100 grid elements (N_x), as presented in Table II.

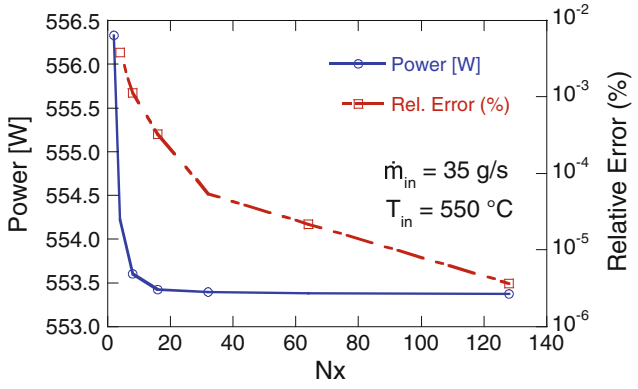

Fig. 5. Grid size dependence of the electrical power generation rate for the baseline model at average inlet conditions. The relative error drops to order of 10^{-5} for 100 grid elements.

RESULTS

Varying Inlet Conditions

The baseline geometry was tested for varying input conditions, i.e., flow rate and inlet temperature, to capture electrical power and pressure drop fluctuations during the engine running cycle. Figure 6 presents the asymptotic trend in electrical power generation with flow rate for the range of 20 g/s to 100 g/s with T_{in} = 550°C. An increased flow rate increases the heat transfer rate through the TEMs with increased power generation; however, the power output saturates at higher flow rates due to heat transfer limitations of the heat exchanger. On the other hand, mass fluxes inside the heat exchanger increase the friction drag forces on the fins and hence increase pressure drops, as shown on the right axis of Fig. 6. The accrued pressure drops were found to be less than the allowed limit. However, the current analysis does not account for recirculation effects near the inlet and exit ports arising due to high area ratios. The spatial variation in flow regimes along the width and height of the thermoelectric generator is also neglected, hence this might not be a true measure of actual device pressure drop.

A similar trend was observed when the inlet exhaust temperature was varied within the range of 400°C to 700°C at average mass flow rate of 35 g/s, as shown in Fig. 7. The electrical power generation rate increases with increasing inlet temperature. The relatively hotter temperatures in the flow region raise the hot-side temperature of the thermoelectric modules, and hence a higher Seebeck voltage is generated across the junctions. The variation in pressure drop with the varying inlet tem-

Table II. Global energy balance for the baseline model at $\dot{m}$ = 35 g/s and T_{in} = 550°C for N_x = 100

Enthalpy Influx, $\dot{H}_{in}$ (W)	Enthalpy Efflux, $\dot{H}_{out}$ (W)	Enthalpy Change, $\Delta\dot{H}$ (W)	Power (el), $\dot{P}_{el}$ (W)	Coolant Heat, $\dot{Q}_{coolant}$ (W)	Energy Transferred, $\dot{Q}_{trf}$ (W)	|Absolute error| (W)	Relative error (%)
29,669.5	19,033	10,636.5	553.4	10,088.6	10,641.9	0.0055	**0.052**

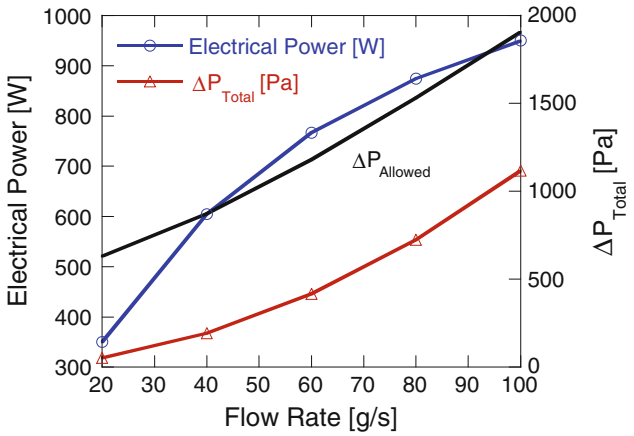

Fig. 6. Electrical power output and associated pressure drops for varying flow rates with T_{in} = 550°C. Power output exhibits an asymptotic trend at higher flow rates. The pressure drop is well within the allowed back-pressure gain (solid line with no markers).

Table III. Calculated thermoelectric parameters from the first control volume of TEG (x = 0) per TEC

I_0 (A)	V_0 (V)	P_0 (W)	R_0 (Ω)	R_{l0} (Ω)	ZT_0
13.9	0.107	0.743	3.89×10^{-3}	3.89×10^{-3}	0.88

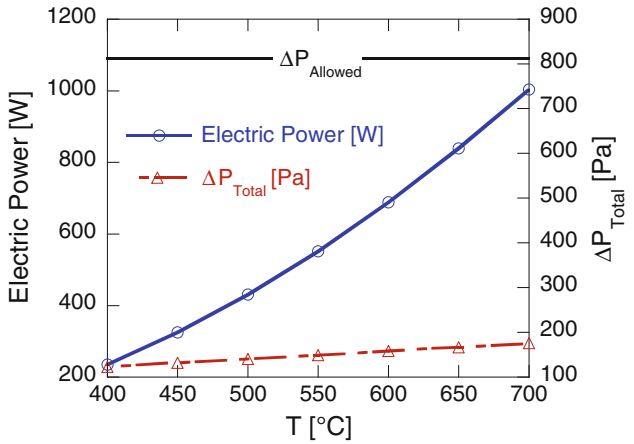

Fig. 7. Power generation rate and associated pressure drop for varying inlet temperatures at $\dot{m}$ = 35 g/s. Electrical power exhibits a strong dependence, whereas the pressure drop variations are negligible.

perature is also presented in Fig. 7. An increase in the air density with higher inlet temperatures tends to increase the channel velocities. This explains the slight increase in the pressure drop with inlet exhaust temperature. The allowed limit for back-pressure rise is 812 Pa at $\dot{m}_{in}$ = 35 g/s, as shown in Fig. 7.

Average Inlet Conditions

Figure 8 presents the temperature drop across various materials in the TEG along its length. It is remarkable to note that there is a difference of more than 100°C between the gas bulk temperature and the hot side of the thermoelectric module. The temperature drop across the hot-side contact by thermal grease is of the order of 30°C. However, the current analysis does not take into account the fin contact resistances, improper surface contacts due to thermally induced deformations, nonuniformity of thermal grease thickness, etc. Hence, the actual temperature drop is expected to be much higher than stated here. The temperature drop across the junctions decreases from 300°C to 120°C. For the skutterudites, ZT values decrease with decrease in temperature, so the modules near the inlet generate more electrical power than those near the rear end, as observed in Fig. 9. This shows that the electrical power generation is highly dependent on the actual

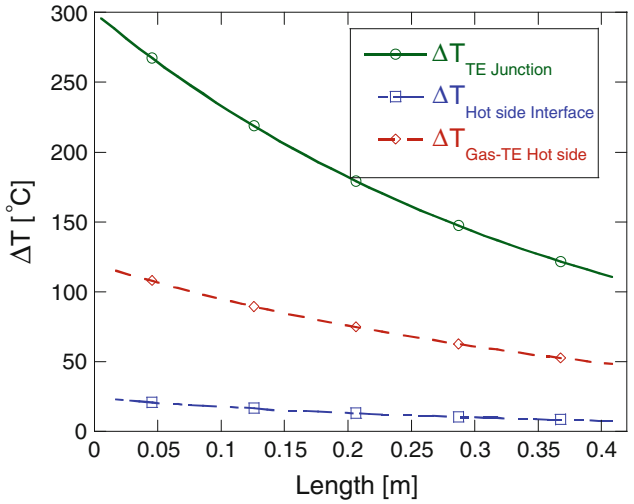

Fig. 8. Variation in temperature drops across materials along the flow direction.

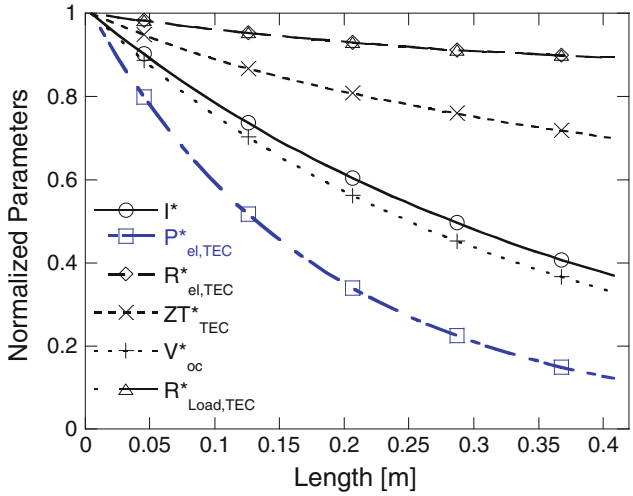

Fig. 9. Variation in normalized thermoelectric parameters along the flow direction. The parameters are normalized by their values from the first computational cell as presented in Table III.

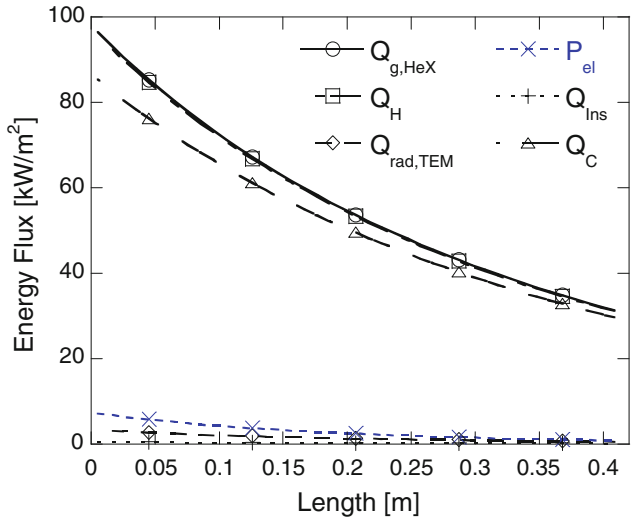

Fig. 10. Variation in energy fluxes on the top (or bottom) surface along the flow direction. The power generating flux shows a continuous decline along the TEG length.

temperature difference across the junctions. The energy fluxes were calculated as the energy transfer rate per unit area from the top surface of the generator. The plot in Fig. 10 presents the decreasing trend in the energy fluxes along the flow direction. The orders of magnitude of the heat leakage due to radiation and the thermal insulation are very low as compared with conduction losses, hence most of the heat transferred by the heat exchanger flows through the thermoelectric modules.

System Efficiency

The pie chart in Fig. 11 presents the energy distribution for the baseline model. The output efficiency of the baseline model in terms of electrical power generation is found to be 3.33% of incident

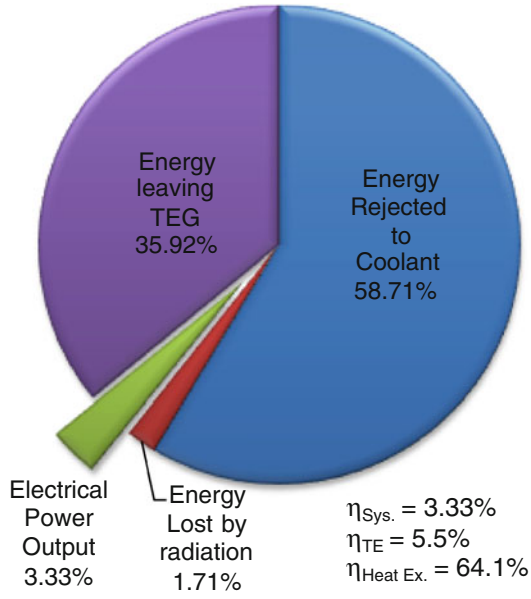

Fig. 11. Pie chart presenting the distribution of energy for the baseline model at average inlet conditions.

energy. Nearly 36% of incident energy leaves the generator to the environment as exhaust gas. Of the incident energy rate, 58% is rejected to the engine coolant system at average inlet conditions. The increased load on the coolant system implies a need for larger engine radiators to reject more heat to the environment. The thermoelectric efficiency of the TEMs was found to be 5.5%, whereas the heat exchanger transfer efficiency was calculated to be 64%.

CONCLUSIONS

A numerical model has been developed to assess and optimize the performance of thermoelectric generators for waste heat recovery in automotive exhaust systems. The model includes the junction averaged temperature-dependent performance of the thermoelectric materials (skutterudite). Performance was assessed for a baseline geometry corresponding to a unit recently evaluated by GM as installed on a Chevrolet Suburban. The performance of this arrangement was studied over a range of operating conditions.

The electrical power generation is observed to be a strong function of flow rate and inlet exhaust temperature. The implications of varying inlet conditions could be very severe if proper conditioning of output power is not carried out. The ZT value of high-temperature skutterudites decreases considerably along the flow direction due to decreasing ΔT and temperatures at the hot-side junction. The thermoelectric modules close to the inlet are exposed to much higher gas temperatures and hence generate higher electrical power output per unit area. By optimizing the fin spacing and thickness, the heat transfer rate can be enhanced con-

siderably. It was found that, at the average inlet conditions, up to 64% of the inlet energy can be transferred through the thermoelectric modules, resulting in a power output of 552 W, approximately 3.33% of the inlet power.

ACKNOWLEDGEMENTS

The authors acknowledge financial support by the National Science Foundation and US Department of Energy (CBET-1048616). We would like to thank Michael Reynolds of GM R&D for helpful discussions and assistance with acquiring the vehicle engine and exhaust data used in this study.

REFERENCES

1. C. Yu and K.T. Chau, *Energy Convers. Manage.* 50, 1506 (2009).
2. F. Stabler, *Proceedings of DARPA/ONR/DOE High Efficiency Thermoelectric Workshop 2002*, pp. 1–26 (2002).
3. J. Yang, *Proceedings of 24th International Conference on Thermoelectrics (ICT) 2005*, pp. 170–174 (2005).
4. D.M. Rowe, *Int. J. Innovations Energy Syst. Power* 1, 13 (2006).
5. D. M. Rowe, *CRC Handbook of Thermoelectrics*, (CRC Press, 1995), pp. 441–458.
6. D.T. Crane and J.W. LaGrandeur, *J. Electron. Mater.* 39, 2142 (2009).
7. G. P. Meisner, *2011 Thermoelectrics Applications Workshop*, San Diego (2011).
8. U. Birkholz, E. Grob, U. Stohrer, K. Voss, D. O. Gruden, and W. Wurster, *Proceedings of 7th International Conference on Thermoelectric Energy Conversion 1988*, pp. 124–128 (1988).
9. E. Takanose and H. Tamakoshi, *Proceedings of 12th International Conference on Thermoelectrics (ICT) 1994*, pp. 467–470 (1994).
10. C. Vinning and D. M. Rowe, *CRC Handbook of Thermoelectrics*, (CRC Press, 1995), pp. 329–337.
11. M.S. Dresselhaus, Y.M. Lin, T. Koga, S.B. Cronin, O. Rabin, M.R. Blackand, and G. Dresselhaus, in *Semiconductors and Semimetals,* ed. By T. M. Tritt (Elsevier, 2001), pp. 1–121.
12. X. Tang, Q. Zhang, L. Chen, T. Goto, and T. Hirai, *J. Appl. Phys.* 97, 093712 (2005).
13. G. Rogl, A. Grytsiv, E. Bauer, P. Rogl, and M. Zehetbauer, *Intermetallics* 18, 57 (2010).
14. D.M. Rowe, *Renewable Energy* 16, 1251 (1999).
15. K. Saqr and M. Musa, *Thermal Sci.* 13, 165 (2009).
16. X.B. Zhao, X.H. Ji, Y.H. Zhang, T.J. Zhu, J.P. Tu, and X.B. Zhang, *Appl. Phys. Lett.* 86, 062111 (2005).
17. C. Suter, P. Tomeš, A. Weidenkaff, and A. Steinfeld, *Materials* 3, 2735 (2010).
18. P. Tomeš, M. Trottmann, C. Suter, M.H. Aguirre, A. Steinfeld, P. Haueter, and A. Weidenkaff, *Materials* 3, 2801 (2010).
19. S. Riffat and X. Ma, *Appl. Therm. Eng.* 23, 913 (2003).
20. N. Espinosa, M. Lazard, L. Aixala, and H. Scherrer, *J. Electron. Mater.* 39, 1446 (2010).
21. K. Chau, Y. Wong, and C. Chan, *Energy Convers. Manage.* 40, 1021 (1999).
22. P. Yodovard, J. Khedari, and J. Hirunlabh, *Energy Sources* 23, 213 (2001).
23. R. Funahashi, *2009 Thermoelectrics Applications Workshop,* San Diego (2009).
24. D.T. Morelli, *Proceedings of 15th International Conference on Thermoelectrics 1996*, pp. 383–386 (1996).
25. A.B. Neild, *SAE Technical Paper 630019* (1963). doi: 10.4271/630019.
26. A.B. Neild, *SAE Technical Paper 670452* (1967). doi: 10.4271/670452.
27. J. Bass, R.J. Campana, and N.B. Elsner, *Proceedings of Annual Automotive Technology Development Contractors Coordination Meeting 1992*, pp. 743–748 (1992).
28. J.C. Bass, N.B. Elsner, and F.A. Leavitt, *AIP Conf. Proc.* 316, 295 (1994).
29. K. Ikoma, M. Munekiyo, K. Furuya, M. Kobayashi, T. Izumi, and K. Shinohara, *Proceedings of 17th International Conference on Thermoelectrics (ICT) 1998*, pp. 464–467 (1998).
30. E.F. Thacher, *2006 Diesel Engine-Efficiency and Emmisions Research (DEER) Conference Presentations,* Detroit (2006).
31. E.F. Thacher, B.T. Helenbrook, M.A. Karri, and C.J. Richter, *Proc IMechE Part D: J. Auto. Eng.* 221, 95 (2007).
32. M.A. Karri, E.F. Thacher, and B.T. Helenbrook, *Energy Convers. Manage.* 52, 1596 (2011).
33. D.M. Rowe, J. Smith, G. Thomas, and G. Min, *J. Electron. Mater.* 40, 784 (2011).
34. A. Eder, J. Liebi, and D. Jänsch, in *Thermoelektrik Eine Chance für die Automobilindustrie* (Renningen, Germany:expert verlag, 2009), pp. 45–56.
35. J. W. Fairbanks, *2011 Diesel Engine-Efficiency and Emissions Research (DEER) Conference Presentations,* Detroit (2011).
36. J. Yang, *2009 Thermoelectrics Applications Workshop*, San Diego (2009).
37. G. P. Meisner, *2011 Diesel Engine-Efficiency and Emissions Research (DEER) Conference Presentations,* Detroit (2011).
38. H. Xiao, X. Gou, and C. Yang, *Proceedings of Asia Simulation Conference*: *7th International Conference on System Simulation and Scientific Computing ICSC 2008*, pp. 1183–1187 (2008).
39. J. Yu and H. Zhao, *J. Power Sources* 172, 428 (2007).
40. F. Meng, L. Chen, and F. Sun, *Energy* 36, 3513 (2011).
41. D.T. Crane, *J. Electron. Mater.* 40, 561 (2010).
42. Y.Y. Hsiao, *Energy* 35, 1447 (2010).
43. K. Matsubara, *Proceedings of 21st International Conference on Thermoelectrics (ICT) 2002*, pp. 418–423 (2002).
44. X.C. Xuan, K.C. Ng, C. Yap, and H.T. Chua, *Int. J. Heat Mass Transf.* 45, 5159 (2002).
45. G. Liang, J. Zhou, and X. Huang, *Appl. Energy* 88, 5193 (2011).
46. B.A. Cola, X. Xu, T.S. Fisher, M.A. Capano, and P.B. Amama, *Nanoscale Microscale Thermophys. Eng.* 12, 228 (2008).
47. B.A. Cola, J. Xu, C. Cheng, X. Xu, T.S. Fisher, and H. Hu, *J. Appl. Phys.* 101, 054313 (2007).
48. B.A. Cola, J. Xu, and T.S. Fisher, *Int. J. Heat Mass Transf.* 52, 3490 (2009).
49. T.J. Hendricks and J.A. Lustbader, *Proceedings of 21st International Conference on Thermoelectrics (ICT) 2002*, pp. 381–386 (2002).
50. C. Baker, P. Vuppuluri, L. Shi, and M. Hall, *J. Electron. Mater.* 41, 1290 (2012).
51. F.P. Incropera and D.P. DeWitt, *Fundamentals of Heat and Mass Transfer,* 6th edn. (Wiley, 2007), pp. 137–168.
52. H. Chanson, *Hydraulics of Open Channel Flow: An Introduction*, 2nd edn., (Butterworth–Heinemann, 2004), p. 231.